Materials for Infrared Windows and Domes

Properties and Performance

SECOND EDITION

DANIEL C. HARRIS

SPIE PRESS
Bellingham, Washington USA

Library of Congress Cataloging-in-Publication Data

Names: Harris, Daniel C., 1948– author.
Title: Materials for infrared windows and domes : properties and performance / Daniel C. Harris.
Description: Second edition. | Bellingham, Washington : SPIE Press, [2024] | Includes bibliographical references and index.
Identifiers: LCCN 2023043887 | ISBN 9781510668843 (hardcover) | ISBN 9781510668850 (pdf)
Subjects: LCSH: Guided missiles–Optical equipment. | Infrared detectors. | Noses (Aircraft)
Classification: LCC UG1310 .H37 2023 | DDC 629.1/2–dc23/eng/20231108
LC record available at https://lccn.loc.gov/2023043887

Published by
SPIE
P.O. Box 10
Bellingham, Washington 98227-0010 USA
Phone: +1 360.676.3290
Fax: +1 360.647.1445
Email: books@spie.org
Web: www.spie.org

Printed in the United States of America.
First printing 2024.
For updates to this book, visit http://spie.org and type “PM368” in the search field.

Contents

Preface *xv*
Acknowledgments *xvii*
About the Author *xix*

1 Optical Properties of Infrared Windows **1**
1.1 Electromagnetic Spectrum and Atmospheric Transmission 2
1.2 Blackbody Radiation 4
1.3 A Day in the Life of a Photon 7
1.4 Refraction and Refractive Index 10
1.4.1 Birefringence 15
1.4.2 Preference for cubic materials 18
1.5 Reflection and Transmission 20
1.5.1 Transmission of an absorbing window 22
1.5.2 Etalon effect 23
1.6 Optical Constants *n* and *k* 26
1.7 Behavior of Absorption Coefficient and Refractive Index 28
1.8 Transmission Spectra of Infrared Materials 30
1.9 Measuring the Absorption Coefficient 43
1.9.1 Direct transmittance measurements 43
1.9.2 Laser calorimetry 46
1.9.3 Photothermal common-path interferometry 49
1.10 Emittance 53
1.10.1 Absorption coefficients of sapphire, spinel, and ALON near their 5 μm absorption cutoff 58
1.11 Effect of Temperature on Absorption and Emission 58
1.12 Free Carrier Absorption in Semiconductors 60
1.13 What Makes a Window Midwave or Long Wave? 67
1.14 "Two-Color" Materials 76
1.15 Infrared Window Absorption Features from Impurities 78
1.15.1 Hot-pressed magnesium fluoride 78
1.15.2 OH in polycrystalline oxides 79
1.15.3 Standard-grade chemical-vapor-deposited ZnS 80
1.15.4 CO_2 trapped in pores of polycrystalline oxide ceramics 80
References 83

2 A Deeper Look into Optical Properties of Windows 89
2.1 Resolution 89
2.2 Optical Scatter 91
2.2.1 Measuring scatter 91
2.2.2 Optical scatter from birefringent polycrystalline materials 97
2.2.3 Model for scatter in birefringent polycrystalline materials 99
2.2.4 Infrared-transparent yttria-stabilized tetragonal zirconia 101
2.3 A Deeper Look at Birefringence 103
2.3.1 Refraction of ordinary and extraordinary rays 104
2.3.2 Double refraction in calcite 107
2.3.3 Normal incidence on *a*-plane sapphire 108
2.3.4 Off-normal incidence on *a*-plane sapphire 110
2.3.5 Birefringence of a sapphire dome 114
2.3.6 Intrinsic birefringence in cubic materials 115
2.3.7 Ordinary and extraordinary absorption coefficients of sapphire 116
2.4 Fresnel Equations 117
2.5 Hemispheric Emissivity 120
2.5.1 Absorptance and emittance 120
2.5.2 Emittance into a full hemisphere 121
2.6 Calculating Spectral Transmittance, Emittance, and Reflectance from Optical Constants 128
2.6.1 Snell's law with a complex index of refraction 129
2.6.2 Transmission and emission of spinel at 1000 K at normal incidence 130
2.6.3 Transmission and emission of spinel at 1000 K at 60° incidence 133
2.7 Modulation Transfer Function: A Measure of Imaging Quality 136
2.8 Degradation of Infrared Sensing by a Hot Window 139
2.8.1 Emittance from a hot window 139
2.8.2 Thermal lensing from temperature gradients in windows 143
2.9 Microwave Transmission Through Infrared Windows 146
2.10 Transmission Through Rain, Snow, Fog, and Dust 150
References 155

3 Mechanical Properties 161
3.1 Elastic Constants 162
3.2 Measuring the Strength of Brittle Materials 166
3.2.1 Three-point flexure test 166
3.2.2 Four-point flexure test 168
3.2.3 Equibiaxial (ring-on-ring) flexure test 172
3.2.4 Pressure-on-ring (hydraulic-burst) flexure test 177
3.2.5 Stronger ceramics tend to break into more pieces 179

3.3 Ceramics Fracture at Pre-existing Flaws 180
3.3.1 Fractography 180
3.3.2 Stress concentration by cracks 185
3.3.3 Larger areas fail at lower stress 188
3.3.4 Strain rate dependence of strength 190
3.4 Hardness 191
3.5 Fracture Toughness 197
3.5.1 Stress intensity factor 197
3.5.2 Measuring fracture toughness 202
3.5.2.1 Single-edge precracked beam 202
3.5.2.2 Surface crack in flexure 204
3.5.2.3 Chevron-notch beam 206
3.5.2.4 Comparison of fracture toughness test methods 207
3.6 Relation of Strength to Fracture Toughness and Grain Size 208
3.7 Hot Forging 211
3.8 Hardness Depends on Grain Size 212
References 214

4 Weibull Statistics and Mechanical Strength 219
4.1 The Weibull Distribution 219
4.1.1 Shape of the Weibull curve 220
4.1.2 Transforming the Weibull equation 222
4.2 Effective Area 223
4.3 Estimating Weibull Parameters from a Logarithmic Plot 226
4.4 Finding Weibull Parameters by the Maximum-Likelihood Method 228
4.5 Weibull Scale Parameter σ_o 234
4.6 Strength Scales with Area (or Volume) Under Stress 235
4.7 Weibull Probability of Survival Without Slow Crack Growth 236
4.8 General Approach to the Weibull Probability of Survival 240
4.9 Strengths of Optical Ceramics 243
4.10 Effect of Temperature on Ceramic Strength 255
4.11 Variability in Strengths of Optical Ceramics 258
4.12 Can We Inspect for Strength? 263
4.12.1 X-ray topography 264
4.12.2 Photon backscattering 266
4.12.3 Dye penetration 267
4.13 Window and Dome Design 267
4.13.1 Design safety factor 267
4.13.2 Designing a circular window 268
4.13.3 Designing a dome 271
4.13.4 Cannon-launched projectile 274
4.14 Maximum-Likelihood Method 276
4.15 Bimodal Weibull Distribution 279
4.15.1 Transforming the Weibull equation 280

4.15.2 Optimizing bimodal Weibull parameters 281
4.16 3-Parameter Weibull Equation 283
4.16.1 Philosophy of the 3-parameter Weibull equation 286
4.16.2 Alternative interpretation of the BK7 strength distribution 287
References 288

5 Thermal Properties 293
5.1 Thermal Expansion 293
5.1.1 Converting the expansion coefficient to $\Delta L/L_0$ 297
5.2 Heat Capacity 300
5.3 Thermal Conductivity 301
5.4 Thermal Shock 306
5.4.1 Hasselman figures of merit 309
5.4.2 Thermal stress analysis and testing 316
5.5 Mach–Altitude Limit for a Dome 320
5.6 Aerodynamic Domes 325
5.7 Thermal Stability of Window Materials 327
References 330

6 Fabrication of Infrared Materials 337
6.1 Classes of Infrared Materials 337
6.1.1 Glass-ceramics 341
6.2 Powder Processing to Make Polycrystalline Optical Materials 343
6.2.1 Structures of spinel and ALON 347
6.2.2 Yttria: an example of dome fabrication from a powder 350
6.2.3 Methods of densifying ceramics: sintering, hot pressing, and hot isostatic pressing 354
6.2.3.1 Hot pressing 356
6.2.3.2 Hot isostatic pressing 357
6.2.4 Annealing 358
6.3 Chemical Vapor Deposition 359
6.3.1 Zinc sulfide and zinc selenide 359
6.3.2 Diamond 366
6.3.2.1 Growth of diamond 367
6.3.2.2 Properties of diamond as an infrared window 370
6.4 Single-Crystal Semiconductor Materials 375
6.4.1 Gallium arsenide, gallium phosphide, germanium, and silicon 376
6.5 Sapphire 379
6.5.1 Heat exchanger method (HEM) for sapphire growth 380
6.5.2 Controlled heat extraction system sapphire growth 382
6.5.3 Gradient solidification sapphire dome growth 383
6.5.4 Edge-defined film-fed growth of sapphire (EFG method) 384
6.5.5 Kyropoulos growth of sapphire 387

6.5.6 Horizontal directional solidification growth of sapphire 389
6.5.7 Effect of twinning on high-temperature strength of sapphire 391
6.5.8 Another twinning phenomenon: Plasticity of zinc sulfide in darkness 397
6.6 Developmental Materials 398
6.6.1 Yttrium aluminum garnet (YAG) 399
6.6.2 Yttria-stabilized tetragonal zirconia (3Y-TZP) 400
6.6.3 Aluminum scandium tungstate as a near-zero-thermal-expansion window 403
References 406

7 Optical Fabrication 419
7.1 Relation of Optical Scatter to Surface Roughness 420
7.2 Scratch/Dig Specification 422
7.2.1 ISO 10110-7 standard for surface imperfections 424
7.3 Optical Finishing 427
7.3.1 Single-point diamond turning 431
7.4 Metrology 432
7.4.1 Interferometry 434
7.4.2 UltraSurf optical coordinate measuring machine 440
7.4.3 Phase-measuring deflectometry 443
7.4.4 The challenge of metrology 445
7.4.5 Fiducial surfaces for freeform optics 446
7.4.6 Structure function for figure error specification 446
7.4.7 Transmitted wavefront error and homogeneity 447
7.5 Origins of Deterministic Grinding and Polishing in the U.S. 449
7.5.1 Deterministic microgrinding 449
7.5.2 Magnetorheological finishing 453
7.6 Advances in Deterministic Finishing after OPTICAM and MRF 466
7.7 Finishing for High Strength 469
7.7.1 Scratches left from grinding 470
7.7.2 Measuring depth of subsurface damage with MRF spot 473
7.7.3 Annealing, flame polishing, and plasma-arc heating 475
7.7.4 Chemical etching 477
7.7.5 Compression for strengthening 478
References 479

8 Optical Coatings 487
8.1 Antireflection Coatings 487
8.1.1 Sub-wavelength structure surface 492
8.1.2 Moth eye surface 492
8.1.3 Interference fringes for measuring coating thickness 497
8.1.4 Random moth eye surface 498
8.1.5 Adherence and weathering of coatings 501

8.1.6 Emittance from coatings 503
8.1.7 Rugate filter 504
8.2 Stress in Coatings 506
8.2.1 Stress in 2-layer composite ZnS|ZnSe window 509
8.2.2 Effect of coating on strength, toughness, and hardness 512
8.3 Conductive Coatings for Electromagnetic Shielding 512
8.3.1 Sheet resistance and continuous coatings 513
8.3.2 Metal grids for electromagnetic shielding 518
References 522

9 Erosion and Impact Protection 529
9.1 Rainfall Characteristics 532
9.1.1 Number of raindrop impacts encountered in flight 535
9.1.2 Shape of a falling raindrop 541
9.2 The Raindrop Impact Event 541
9.2.1 Relation of rain impact force to drop size and impact speed 546
9.3 Rain Erosion Test Facilities 547
9.3.1 Whirling arm 547
9.3.2 Single-impact waterjet 550
9.3.3 Multiple-impact jet apparatus (MIJA) 551
9.3.4 Single-drop impact testing 554
9.4 Raindrop Damage Threshold Velocity 556
9.4.1 Threshold velocity for fracture or loss of mechanical strength 556
9.4.2 Pre-existing flexure stress in a window enhances erosion 561
9.4.3 Threshold velocity for loss of optical transmission 561
9.4.4 Threshold velocity for loss of mass 564
9.5 Aerodynamic Effects in Rain Erosion 565
9.5.1 Fresh aerodynamic simulations 568
9.5.2 What was wrong with previous assessments? 570
9.6 Erosion by Solid Particles 572
9.6.1 Sources of variability in sand erosion testing 577
9.6.2 Combined effects of sand and rain 582
9.7 Sand Impact Damage Model in Materials Softer than Sand 582
9.7.1 Description of sand impact damage 582
9.7.2 Model for optical transmission loss by sand impact 585
9.8 Thermal Stress from Raindrop Impact on a Hot Dome 589
9.9 Effect of Angle of Incidence on Erosion 594
9.9.1 Waterdrop impact at inclined angles 594
9.9.2 Sand impact at inclined angles 595
9.9.3 Comparative erosion testing of materials 596
9.10 Protective Coatings for Erosion 597
9.10.1 Mechanisms of protection by coatings 598

9.10.2 Protective cladding with compliant interface 601
9.10.3 Diamond-like carbon and germanium-carbon coatings 604
9.10.4 Boron phosphide and other phosphorus-based coatings 606
9.10.5 REP coating 612
9.10.6 Claddings 613
9.10.7 Diamond coatings 618
References 622

10 Slow Crack Growth 633

10.1 Slow Crack Growth 633
10.1.1 A little humility 638
10.1.2 Fatigue limit and threshold strength 640
10.1.3 Effect of humidity and temperature on slow crack growth 642
10.1.4 Slow crack growth in sapphire 647
10.2 Examples of Dynamic Fatigue Measurements 647
10.2.1 Dynamic fatigue of BK7 glass 649
10.2.2 Dynamic fatigue of as-polished zinc sulfide 652
10.2.3 Dynamic fatigue of indented fused silica 655
10.2.4 Preloading saves time in dynamic fatigue measurements 658
10.3 Fracture Mechanics of Slow Crack Growth 660
10.3.1 Power law equation for strength loss 661
10.3.2 Power law parameters from static fatigue 663
10.3.3 Exponential law equation for strength loss 666
10.3.4 Time to failure from static fatigue 667
10.3.5 Power law time to failure from static fatigue 667
10.3.6 Exponential law time to failure from static fatigue 669
10.3.7 Exponential law parameters from static fatigue 670
10.3.8 Key results from Section 10.3 673
10.4 Dynamic Fatigue Analysis 674
10.4.1 Dynamic fatigue of as-polished coupons to find power law parameters 674
10.4.2 Dynamic fatigue of indented coupons 677
10.4.2.1 Stress intensity field for indented coupons 678
10.4.2.2 Evolution of K_I and crack size in dynamic fatigue of indented and as-polished coupons 680
10.4.2.3 Spreadsheet for dynamic fatigue of indented coupons 683
10.4.3 Spreadsheet for dynamic fatigue of unindented coupons 686
10.5 Dynamic Fatigue Data Analysis Without a Computer Program 689
10.5.1 Case 2. Approximate method to find power law from dynamic fatigue of indented coupons 689
10.5.2 Case 3. Approximate method to find exponential law from dynamic fatigue of indented coupons 692

10.5.3 Case 4. Approximate method to find exponential law from dynamic fatigue of unindented coupons 694
10.5.4 Summary of dynamic fatigue data analysis 697
References 697

11 Proof Testing and Window Lifetime 701
11.1 Proof Test Stress Profile 702
11.1.1 Verify the fidelity of a proof test with strain gauges or test a full-scale vehicle 708
11.2 Good, Bad, and Ugly Proof Tests 709
11.2.1 When slow crack growth occurs in the proof test 711
11.2.2 When a proof test fails to improve the strength of survivors 713
11.2.3 How fast does proof test unloading need to be? 715
11.2.4 Is heptane an inert environment? 718
11.3 NASA Window Design Rules for Manned Systems 718
11.4 Applying NASA Window Design Rules for Fused Silica 720
11.4.1 Steps for NASA design life calculation 723
11.4.2 Select design life, minimum time to failure, operating parameters, and material parameters 724
11.4.3 Calculate maximum tensile surface stress σ_{app} in the window 724
11.4.4 Calculate t_{fail} for a range of K_{Ii} values and select K_{Ii} to achieve desired t_{fail} 725
11.4.5 Calculate initial flaw size to achieve desired t_{fail} 726
11.4.6 Calculate initial strength to achieve desired t_{fail} 726
11.4.7 Proof stress 727
11.4.8 Probability of failure in a proof test and expected strength of the window 727
11.4.9 Proof test to ensure that window has at least minimum required strength for intended service life 728
11.4.10 Assessment of fused silica design 729
11.4.11 Power law versus exponential law time to failure 731
11.4.12 Observed relation of strength to flaw depth 731
11.5 Applying NASA Window Design Rules for Zinc Sulfide 733
11.5.1 Calculate t_{fail} for a range of K_{Ii} values 734
11.5.2 Strategies to increase an insufficient design life 734
11.5.3 Relaxing NASA standards to increase design life 737
11.5.4 ZnS slow crack growth measured in 1993 738
11.5.5 Summary of ZnS window design 740
11.6 Slow Crack Growth Parameters for Infrared Materials 742
11.7 Proof Test Diagram 752
11.7.1 Equations for the proof test diagram 754
11.7.2 Summary 754
References 755

Appendices **757**

A. Physical Constants, Conversion Factors, and SI Units and Prefixes 757
B. Optical Properties of Infrared Materials 761
C. Radiometry Definitions 795
D. Elastic Constants 799
E. Engineering Properties of Selected Materials 809

Index *843*

After finishing work on windows, Dan begins the floors.

Preface

This text provides a comprehensive introduction to infrared-transparent materials that must withstand harsh environmental conditions, such as high-speed flight or high-temperature process monitoring. Each section contains sufficient introductory explanation to be readable by a person with a background in science or engineering. The book is also a reference on window material properties.

This book is written from the engineering orientation of "How do we use these materials?" For an outstanding, complementary book written from a science viewpoint, I call your attention to A. Goldstein, A. Krell, and Z. Burshtein, *Transparent Ceramics* (American Ceramic Society/Wiley, 2020).

The present volume builds on its two predecessors: (1) *Infrared Window and Dome Materials*, published in 1992 in the SPIE Tutorial Text series, and (2) *Materials for Infrared Windows and Domes: Properties and Performance*, published in 1999 in the SPIE Press Monograph series. Each volume was double the length of its predecessor, a trend which, I think, reflects some law of thermodynamics. That trend also reflects my learning as I worked in the field more years on a wider variety of projects, learned from my professional colleagues, and taught a short course on windows and domes 60 times at professional conferences and at China Lake.

The book you are reading has expanded coverage of optical properties of windows in Chapters 1 and 2. Most of Chapter 2 is new to this edition as I learned about birefringence, Fresnel equations, hemispheric emissivity, and calculating spectral transmittance, emittance, and reflectance from complex optical constants. In every chapter, I try to teach subject matter through numerical examples. Chapter 3 expands the coverage of mechanical properties of ceramics. Chapter 4 on Weibull statistics applies the ASTM maximum-likelihood method to characterize the strength of brittle materials. I have added what I learned about bimodal strength distributions and apparent threshold strengths below which some materials do not seem to fail (we wish!).

Chapter 6 on fabrication of materials emphasizes the most used materials. Emerging materials such as infrared-transparent polycrystalline alumina and a nanocomposite optical ceramic are included. Diamond is put in perspective

as a material with unique properties, but its cost still limits its use. A few developmental materials are described. Chapter 7 discusses optical finishing. Some history of the development of deterministic grinding and polishing in the U.S. is recounted. This development led to today's Magnetorheological Finishing®, UltraForm Finishing®, ultrasonic machining, UltraSurf Metrology®, and the capability to make free-form optics. Chapter 8 describes antireflection coatings and surfaces, and electromagnetic shielding.

Chapter 9 on erosion by rain and sand discusses rainfall characteristics and the rain impact event. The physical origin of the raindrop size distribution is described. A section based on the latest work in fluid dynamics contradicts the widely held belief that significant drop distortion occurs prior to impact on a dome in supersonic flight. Another new section estimates the localized thermal stress produced when a raindrop collides with a hot window. A physical model for loss of transmission from sand erosion is presented. Erosion-protection coatings are described, but, alas, I found little new published information on this subject.

Chapters 10 and 11 on slow crack growth, window lifetime, and proof testing are entirely new in this edition. The last five years of my Navy career were heavily focused on window design of operational systems subject to slow crack growth. I try to teach computations that were very challenging for me to decipher from the research literature. Appendices contain expanded information on optical and thermal properties of window materials.

I began to write this edition in 2015–2016, but there was not enough time to complete it before it was overtaken by other work. After retiring from the Navy in 2022, writing this book occupied the next two years of my life. I thoroughly enjoyed working on this book. I hope it will be a continuing resource for engineers and scientists who design and build systems with sensor windows that must operate in harsh conditions.

Dan Harris March 2024
China Lake, California
dan_harris@alum.mit.edu

Acknowledgments

My wife Sally contributes to every aspect of the production of the books I have written, and she produced most of the finished illustrations in my SPIE Press books. She produced pen-and-ink drawings (before computers) for our first book, *Symmetry and Spectroscopy*, which was written when we were students. Those illustrations were done on a drafting board with a toddler looking over her shoulder and our second child still in the womb. The current book is our nineteenth.

I have been blessed with a long string of capable, caring managers in the Research Department at China Lake. I particularly thank Alan Van Nevel and Steve Fallis, who were the final members in this string. My first manager, Bob Schwartz, introduced me to windows and domes.

Linda Johnson at China Lake recorded most of the original transmission spectra in this book. Theo Theofanous (Theofanous & Co. and formerly University of California Santa Barbara) drafted sections of this book on distortion of raindrops in the flow field of a dome and on thermal stress from raindrops colliding with hot domes. Mary Ray and Mara Bowen at the China Lake Technical Library provided journal articles without which this book could not have been written.

People who reviewed parts of this book were Colin Ryan (China Lake), Howard Poisl (formerly Raytheon), Stephanie Bell (Raytheon), John McCloy (Washington State University), Lee Goldman (Surmet), Mike Thomas (Applied Physics Lab), and Kendall Johnson (Space Dynamics Lab) along with two anonymous SPIE reviewers. Tom Hartnett (Raytheon and Surmet) provided much information.

Over the years, I learned about ceramics and their behavior from colleagues in industry and the Defense Department. Rick Gentilman at Raytheon and Bill Rhodes at GTE Labs were my first "instructors." More recent industrial colleagues were Mark Parish and Marina Pascucci at CeraNova Corp. It is not a coincidence that Bill Rhodes and Marina Pascucci have both served as President of the American Ceramic Society. At China Lake, Hal Bennett and Jean Bennett tutored me in some optical properties of materials. Jean was a President of the Optical Society of America. Bill Adler of General Research Corp. was a pioneer in the study of raindrops interacting

with windows and domes, and was a cherished colleague. Mike Thomas, Bill Tropf, and Kelly Frazer at the Johns Hopkins University Applied Physics Laboratory were valuable resources for me.

My Navy colleagues included Roger Sullivan, Lee Cambrea, Colin Ryan, Sung Choi, Ray Delcher, Linda Johnson, Mark Moran, Wayne Weimer, Mike Seltzer, Marian Hills, Dick Compton, Rick Burnes, Doug Ricks, Bob Pyke, Curtis Martin, and Inna Talmy. Army colleagues included Jim Kirsch, Brian Jones, Bruce Moylan, Gary Gilde, and Parimal Patel. Air Force colleagues included Butch Porter, Brian Anderson, David Zelmon, and, way back when I started out, Gordon Griffith. My NASA colleagues Perry Gray, Jon Salem, and Lynda Estes and NIST colleagues Ed Fuller and George Quinn taught me a great deal.

Industry colleagues from whom this book benefits are Chuck Willingham, Randy Tustison, Tom Hartnett, Claude Klein, Ralph Korenstein, Wayne Sunne, David Knapp, Howard Poisl, Brian Zelinsky, and Jim Gottleib, all from Raytheon. John McCloy from Raytheon and now at Washington State University is an expert on zinc sulfide. Lee Goldman and Rich Twedt from Surmet have been invaluable sources of knowledge on aluminum oxynitride and spinel ceramics. Larry Fehrenbacher of TA&T shared a great deal of his knowledge of spinel. Other key colleagues were Joel Askinazi from the Danbury, Connecticut optics integrator (which was formerly Perkin-Elmer but had half a dozen different owners during my career) and Paul Klocek from Texas Instruments (which is now Raytheon).

My education in optical finishing is largely from Mike Bechtold, Ed Fess, Scott DeFisher, and others at OptiPro, from Jessica DeGroote Nelson and others at Optimax, Jeff Ruckman (Lockheed Martin), Ted Turnquist (Meller Optics), and Marc Tricard, Aric Shorey, and William Kordonski (QED Technologies).

My education in sapphire growth and properties came largely from Fred Schmid (Crystal Systems), John Locher and Harry Labelle, Jr. (Saphikon), Elena Dobrovinskaya (Rubicon), and Atara Horowitz (Rotem).

My editor Dara Burrows at SPIE Press contributed to the format and clarity of this book and was a true pleasure to work with.

About the Author

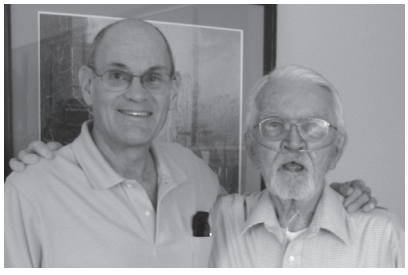

Dan with Don Roy (1924–2015) in 2015. Don was widely considered "father of spinel" at Coors Ceramics and played an important role in developing the hot pressed infrared window materials MgF_2, ZnS, and ZnSe at Kodak.

Dan with Steve Jacobs (1948–2015) in 2011. Steve was a Senior Scientist in the Laboratory for Laser Energetics at the University of Rochester, as well as Professor in the Institute of Optics, Chemical Engineering, and the Materials Science Program. He evaluated magnetorheological finishing in Belarus in 1992 and helped develop that technology into a commercial capability in the U.S.

Daniel C. Harris retired in 2022 from his position as Senior Scientist and Esteemed Fellow in the Research Department at the Naval Air Warfare Center at China Lake, California, where he specialized in infrared window and dome materials for 38 years. He earned a Bachelor's degree in Chemistry from Massachusetts Institute of Technology in 1968 and a Ph.D. in Chemistry from California Institute of Technology in 1973. Prior to coming to China Lake, he taught at the University of California at Davis and at Franklin & Marshall College in Lancaster, Pennsylvania. He authored the widely used undergraduate analytical chemistry textbooks *Quantitative Chemical Analysis* (10th edition, 2020) and *Exploring Chemical Analysis* (5th edition, 2013) and co-authored *Symmetry and Spectroscopy* (1978), which remains in print in 2024.

Chapter 1
Optical Properties of Infrared Windows

All objects above absolute zero temperature emit infrared radiation. This radiation can be used to measure the temperature of an object or can be used to observe military targets. "Heat-seeking" missiles use infrared radiation from the hot exhaust of a target aircraft to guide themselves to the target.

The nose of the infrared-guided missile in Fig. 1.1 is a hemispheric, infrared-transparent dome made of magnesium fluoride. The ceramic dome protects a delicate, hermetically sealed infrared seeker from the harsh environment of high-speed missile flight. The dome must withstand rapid aerothermal heating when the missile is launched and must resist long-term erosion from raindrops and dust encountered during captive carry of the missile beneath the wing of an aircraft.

This book discusses optical, mechanical, and thermal properties of infrared window and dome materials. It describes fabrication techniques and

Figure 1.1 Nose of a Sidewinder missile showing the dome that protects the infrared seeker. (Photograph courtesy of Naval Air Warfare Center, China Lake, California.)

coatings required to enhance optical transmission and mechanical durability. The last chapter considers slow crack growth in window design. We emphasize the few materials capable of external use in demanding environments.

1.1 Electromagnetic Spectrum and Atmospheric Transmission

Electromagnetic radiation is characterized by a *frequency* ν (number of oscillations of the electric field per second) and *wavelength* λ (distance between crests of the electric field). The speed of light c is the product of wavelength and frequency:

$$c = \lambda\nu. \tag{1.1}$$

The speed of light in vacuum is exactly 2.997 924 58×10^8 m/s (which defines the length of a meter). The energy E of a photon (a "particle" of light) is proportional to its frequency, and inversely proportional to its wavelength:

$$E = h\nu = \frac{hc}{\lambda}. \tag{1.2}$$

The constant of proportionality, *Planck's constant*, is $h = 6.626\,070\,15 \times 10^{-34}$ J·s. Physical constants and conversion factors are listed in Appendix A.

Table 1.1 shows names, wavelengths, and frequencies for various parts of the electromagnetic spectrum. Infrared wavelengths are often expressed in micrometers, μm (10^{-6} m), and visible wavelengths are typically given in nanometers, nm (10^{-9} m). Infrared radiation spans the wavelength range 0.78

Table 1.1 Electromagnetic spectrum.

Radiation type	Wavelength		Frequency ($s^{-1} \equiv$ hertz = Hz)
Gamma rays	$<10^{-11}$ m		$>3 \times 10^{19}$
X-rays	10^{-11}–10^{-8} m		3×10^{19}–3×10^{16}
Ultraviolet	10^{-8}–3.8×10^{-7} m		3×10^{16}–7.9×10^{14}
Visible	3.8×10^{-7}–7.8×10^{-7} m		7.9×10^{14}–3.8×10^{14}
Violet	380–430 nm	Yellow	530–580 nm
Blue	430–480 nm	Orange	580–620 nm
Green	480–530 nm	Red	620–780 nm
Infrared (IR)	0.78–1000 μm		3.8×10^{14}–3×10^{11}
Near IR	0.9–1.7 μm	Midwave IR	3–5 μm
Short wave IR	2.0–2.5 μm	Long wave IR	8–14 μm
Terahertz	0.1–1 mm		3×10^{12}–3×10^{11}
Microwave	10^{-3}–10^{-1} m		3×10^{11}–3×10^{9}
Radio	$>10^{-1}$ m		$<3 \times 10^{9}$

to 1000 μm. Visible radiation has higher energy than infrared, while microwave radiation has lower energy.

Figure 1.2 is a transmission spectrum of the atmosphere, with absorption features by various atmospheric constituents noted. The transmittance of a perfectly transparent medium is 100%, while an opaque medium has a transmittance of 0%. In Fig. 1.2, we see a transmission window in the visible region (below 0.7 μm) and several windows in the infrared. Atmospheric transmission varies with pathlength (how far you are looking through the atmosphere), altitude, and humidity. Regions for infrared sensing are the *long wave infrared window* between 8 and 14 μm, the *midwave infrared window* from 3 to 5 μm, and the *near-* and *short-wave infrared windows* from about 0.9 to 2.5 μm. The midwave window is interrupted by a strong absorption band from carbon dioxide near 4.3 μm. Whereas midwave and long wave radiation are emitted by warm objects, short-wave infrared radiation is mainly reflected sunlight and can produce images similar in contrast and detail to visible images.

At the top of Fig. 1.2 is a *wavenumber* scale. Wavenumber is the reciprocal of wavelength, with cm^{-1} being the most common unit:

$$\text{Wavenumber} \equiv \frac{1}{\lambda}. \tag{1.3}$$

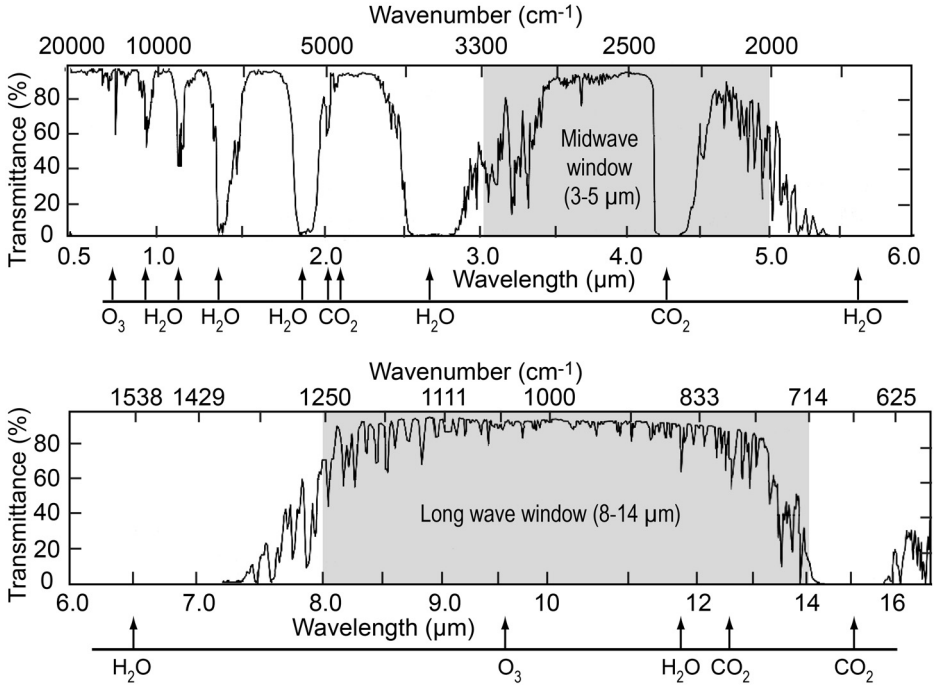

Figure 1.2 Infrared transmission spectrum of the atmosphere for a 1 km path at sea level at 15°C with 46% relative humidity. (Adapted from Santa Barbara Research Center data.)

1.4.1 Birefringence

A birefringent crystal has two different refractive indices and refracts randomly polarized light into two rays, forming the double image shown for calcite in Fig. 1.10. Calcite has two very different refractive indices. Most birefringent materials do not split an image as much as calcite does.

We say that glass is *isotropic* because its optical (and other) properties are the same in every direction. Crystalline materials have a regular structure in which different directions may be physically distinct. In crystals with a cubic structure, such as the sphalerite form of zinc sulfide, optical properties are the same in every direction. Crystals with lower symmetry than cubic, such as calcite or sapphire in Fig. 1.11, are *anisotropic*. That is, they have two or three distinct directions with different optical properties. Sapphire has *axial symmetry* with a unique direction (the *c* direction) having 3-fold rotational symmetry.

Figure 1.12 shows *plane-polarized* electromagnetic radiation (a light ray) traveling in the *x* direction. The electric field oscillates in just one plane (*xy* in this illustration) perpendicular to the direction of travel. The magnetic field oscillates in the *xz* plane. *Randomly polarized* light has equal components of the electric field oscillating in the *xy* and *xz* planes.

Plane-polarized light rays passing through sapphire or any axially symmetric crystal are classified as ordinary or extraordinary. *The electric field of an ordinary ray oscillates perpendicular to the axis of highest symmetry* (*c*), which is called the *optic axis*. Every ray traveling in the *c* direction has its electric field oscillating perpendicular to *c* ($E \perp c$) and is an *ordinary ray*. Every plane polarized ray traveling in any direction with the plane of its electric field perpendicular to *c* is an ordinary ray. Figure 1.13(a) shows one ordinary ray traveling in the *am* plane with *E* plane $\perp$ *c* and another ordinary ray traveling at angle ϕ with respect to the *c* axis with $E \perp c$. *The refractive index for every ordinary ray is* n_o, the *ordinary refractive index*.

Figure 1.10 Birefringence of calcite splits the word beneath the crystal into two images. (Photograph by Sally Harris.)

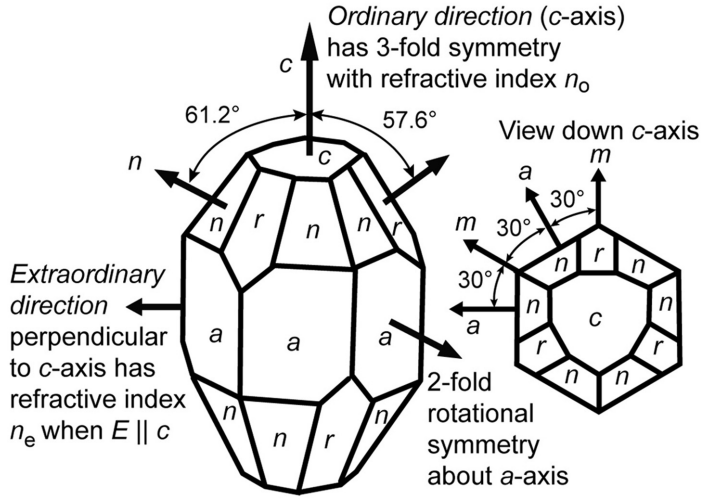

Figure 1.11 Sapphire crystal showing 3-fold (*c*-axis) and 2-fold (*a*-axis) symmetry directions and cleavage faces. The *c*-axis is normal (perpendicular) to the *c*-plane, the *a*-axis is normal to the *a*-plane, and the *m*-axis is normal to the *m* plane. The electric field of a light ray traveling along the *c* direction oscillates perpendicular to the *c* direction.

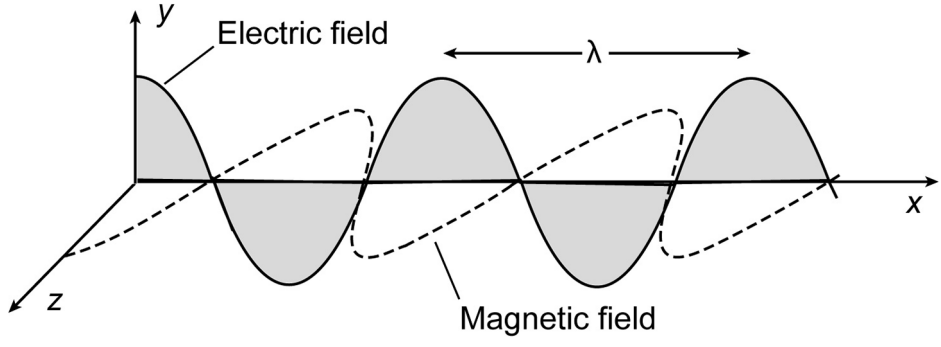

Figure 1.12 A *plane-polarized* light ray of wavelength λ traveling in the *x* direction with the electric field oscillating in the *xy* plane.

One ray traveling in the *am* plane in Fig. 1.13(a) is polarized with its electric field oscillating parallel to *c* ($E \parallel c$). This ray is an *extraordinary ray* with refractive index n_e.

The ray traveling at angle ϕ with respect to the *c* axis is redrawn in Fig. 1.13(b). The plane containing the optic axis and the light ray is called a *principal plane*. Figure 1.13(b) shows that an ordinary ray is polarized with its electric field oscillating perpendicular to the principal plane. The refractive index of every ordinary ray traveling in any direction is n_o. Figure 1.13(b) shows that an extraordinary ray is polarized with its electric field oscillating in

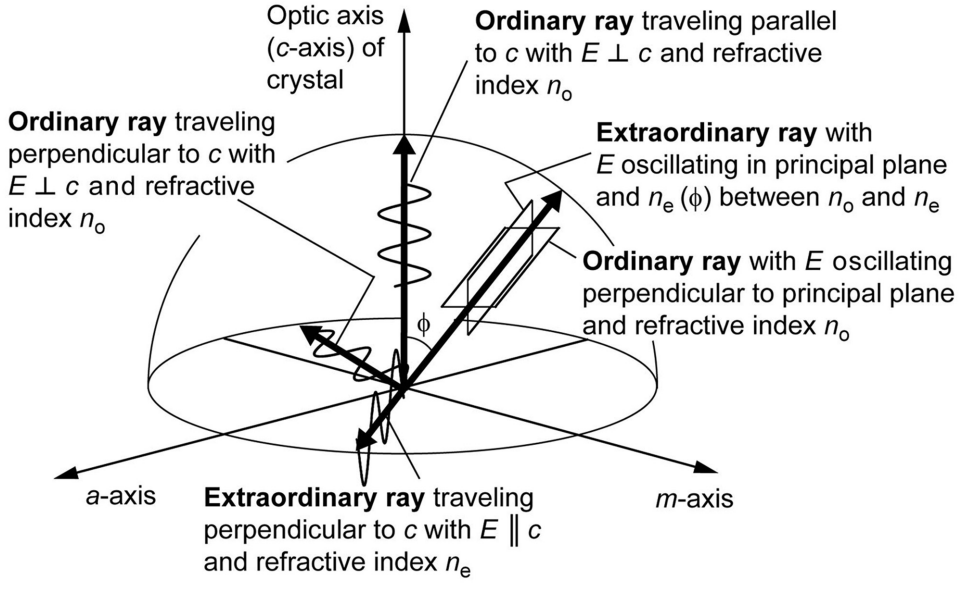

(a)

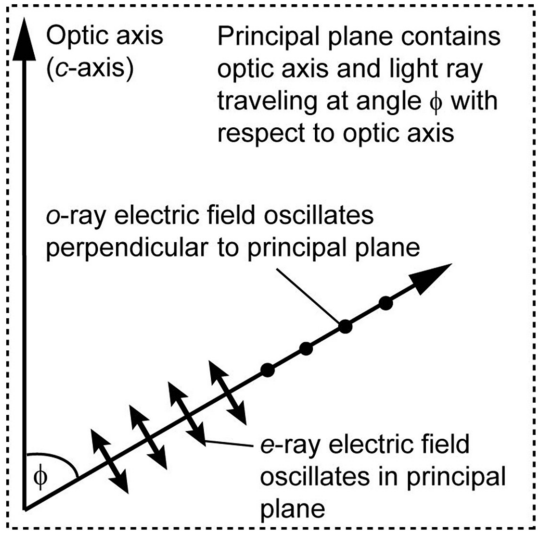

(b)

Figure 1.13 (a) The electric field of an *ordinary ray* oscillates in a plane perpendicular to the optic axis (*c*-axis). (b) The electric field of an *extraordinary ray* oscillates in the principal plane, which includes the optic axis and the light ray vector.

the principal plane. The refractive index of the extraordinary ray lies between n_e and n_o, depending on the angle ϕ. Equation (2.7) in Chapter 2 gives the dependence of the extraordinary refractive index $n_e(\phi)$ on the angle ϕ. The extraordinary ray traveling in the *am* plane in Fig 1.13(a) perpendicular to

Chapter 3
Mechanical Properties

Infrared window and dome materials are classified as *ceramics*, which is a broad term encompassing inorganic, nonmetallic materials. Ceramics are typically brittle, stable at high temperature, and poor conductors of heat and electricity. In this chapter we discuss the mechanical behavior of brittle materials, which are somewhat different from ductile metals.

Figure 3.1 shows specimens of yttria (yttrium oxide, Y_2O_3) fabricated for a test of tensile strength. Each piece was gripped at the ends and pulled apart until it broke. If these had been metal, they would have broken in the narrow section near the middle (called the *gage section*), and all failures would have occurred at nearly the same load. Instead, three of five samples broke in the thick end region, and the load at failure varied by >20%.

Optically polished ceramics usually fail at flaws such as scratches at or near the surface of the material. Residual damage at or beneath the surface left from grinding and polishing is frequently the source of failure. Some ceramics have strength-limiting inclusions of foreign material or small internal voids.

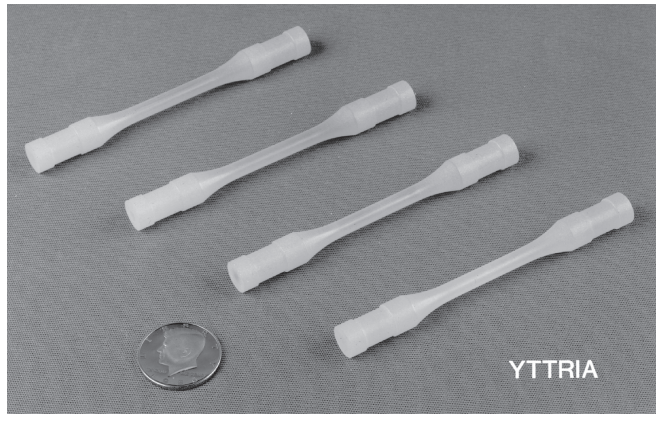

Figure 3.1 Yttria "dog bone" specimens with a 0.4-cm-diameter central gage section, prepared for tensile strength measurement. (Photograph courtesy of Raytheon Co.)

3.1 Elastic Constants

Consider a cylinder of solid material gripped at the ends and pulled apart until it breaks. The force per unit area pulling on the object is called the *stress* σ:

$$\text{Stress} = \sigma \equiv \frac{\text{force}}{\text{area}}. \tag{3.1}$$

The symbol $\equiv$ means "is defined as." Area in Eq. (3.1) is the cross-sectional area of the cylinder. Units of stress are newtons per square meter, known as *pascals* ($\text{Pa} = \text{N/m}^2$). The English units of stress are pounds per square inch (psi). A common abbreviation for 1000 psi is *ksi*. The relation between the English and metric units is $1 \text{ ksi} \approx 6.895 \text{ MPa}$ ($\text{M} = \text{mega} = 10^6$). For example, a stress of 5.3 ksi is equivalent to $5.3 \text{ ksi} \times 6.895 \text{ MPa/ksi} = 37 \text{ MPa}$.

If the cylinder has a length ℓ before force is applied, and length $\ell + \Delta\ell$ when stretched, we say that the *strain* ε is the fractional increase in length:

$$\text{Strain} = \varepsilon \equiv \frac{\Delta\ell}{\ell}. \tag{3.2}$$

Figure 3.2 shows the behavior of brittle and ductile materials when tensile stress is applied. The brittle material stretches slightly, with strain proportional to stress: if stress is doubled, the strain doubles. Eventually the stress reaches the strength of the material and fracture occurs. The *strength* of the material is the stress at failure. The slope of the stress versus strain curve is called *Young's modulus E*:

$$\text{Young's modulus} = E \equiv \frac{\text{stress}}{\text{strain}} = \frac{\sigma}{\varepsilon}. \tag{3.3}$$

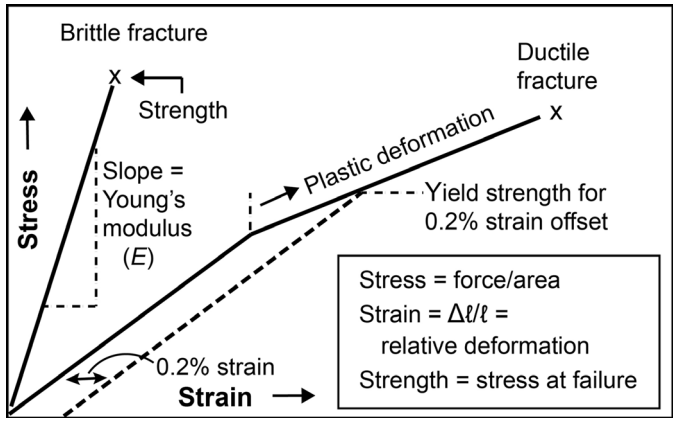

Figure 3.2 Schematic response of brittle and ductile materials to tensile stress.

The greater the value of Young's modulus, the stiffer the material. That is, a greater stress is required to produce a given strain. The behavior of the brittle material in Fig. 3.2, prior to fracture, is said to be *elastic*. When stress is removed, the material returns to its original shape.

Figure 3.2 also shows stress–strain behavior for a ductile material such as a metal. Initial elastic deformation is followed by a region of *plastic deformation* in which the object does not return to its original dimensions if stress is removed. The *yield strength* of a ductile material is often taken as the stress at the intersection between the stress–strain curve and the 0.2% strain offset line.

Figure 3.3 shows a cylindrical solid with initial length ℓ and initial diameter d. After a tensile stress σ is applied, the length increases to $\ell + \Delta\ell$ and the diameter shrinks to $d - \Delta d$. *Poisson's ratio* ν (pronounced **pwa**-san) is the fractional change in diameter divided by the fractional change in length:

$$\text{Poisson's ratio} = \nu \equiv \frac{\Delta d/d}{\Delta\ell/\ell}. \tag{3.4}$$

Ceramic materials undergo an *elastic deformation* for which Poisson's ratio is typically ~0.2–0.3. A material that exhibits plastic (viscous) flow or creep maintains a constant volume as it distorts. In such a case, Poisson's ratio is 0.5.

Obtaining Stress–Strain Data by a Common Method

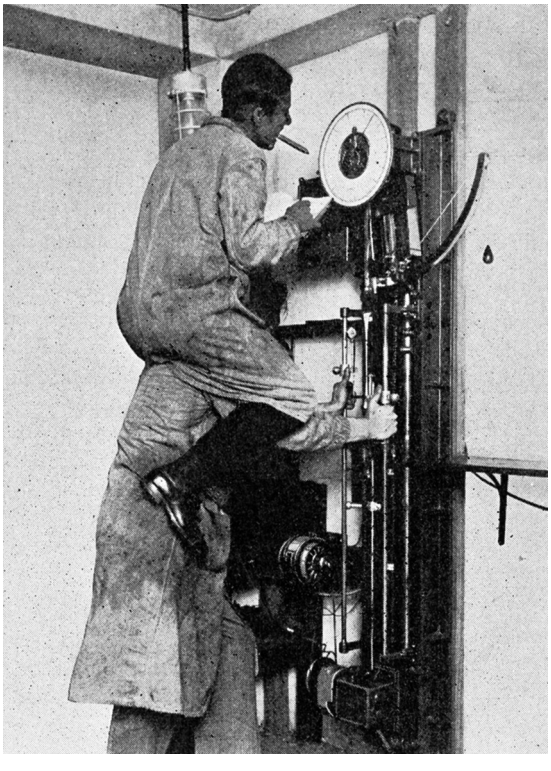

From A. A. Somerville, J. M. Ball, and L. A. Edland, "Autographic stress-strain curves of rubber at low elongations," *Ind. Eng. Chem., Analytical Ed.* **2**, 289–293 (1930).

A thickness of 2 mm is between 0.70 and 3.18 mm. The quotient $(c - b)/d$ in Eq. (3.19) is $(19 - 15.875)/2 = 1.56$, which is in the allowed range of 1 to 6. If we had increased the disk radius to $c = 25$ mm, the dimensions would still be allowable and the stress at the edge of the disk would be reduced.

The purpose of the equibiaxial flexure test is to measure the strength of the polished face of the test specimen. Therefore, the specimen should be polished by the same set of steps with the same abrasives that will be used to polish a full-size window. Faces should be flat and parallel to within 0.05% of the disk diameter, which is 0.019 mm for a diameter of 38 mm. The edge of the disk should be fine ground and may be chamfered.

The stress rate for an equibiaxial flexure test is equivalent to that given by Eqs. (3.10) and (3.11) for uniaxial flexure:

$$\text{Stress rate}\,(\mathrm{N}/[\mathrm{m}^2 \cdot \mathrm{s}]) = \frac{6Eds}{(2b)^2}, \tag{3.20}$$

where E is Young's modulus, d is the disk thickness, s is the crosshead speed of the test machine, and $2b$ is the support diameter. A common crosshead speed of 0.508 mm/min in Eq. (3.20) gives a stress rate of 27 MPa/s for spinel with a thickness of 2 mm and support radius of 15.875 mm.

3.2.4 Pressure-on-ring (hydraulic-burst) flexure test

A pressure-on-ring test (Fig. 3.13) measures the strength of a window in a manner that mimics uniform pressure loading of a real window. A disk is supported on one side by a ring and uniformly loaded from the other side by hydraulic pressure. The specimen may be separated from the hydraulic fluid by a neoprene diaphragm with a thickness such as 1.6 mm.[13] Radial and hoop components of stress at radial position r within support radius b ($r \leq b$) are:[14]

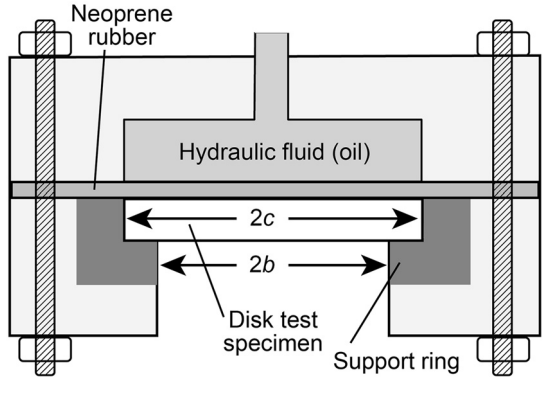

Figure 3.13 Pressure-on-ring (hydraulic-burst) test applies uniform hydraulic pressure P to one face of a test disk of radius c with support radius b and thickness d. (Adapted from Matthewson and Field.[13])

$$\text{Radial stress} = \frac{3Pb^2}{8d^2}\left[(1-\nu)\left(\frac{b^2}{c^2}\right) + 2(1+\nu) - (3+\nu)\left(\frac{r^2}{b^2}\right)\right] + \frac{(3+\nu)P}{4(1-\nu)} \tag{3.21}$$

$$\text{Hoop stress} = \frac{3Pb^2}{8d^2}\left[(1-\nu)\left(\frac{b^2}{c^2}\right) + 2(1+\nu) - (1+3\nu)\left(\frac{r^2}{b^2}\right)\right] + \frac{(3+\nu)P}{4(1-\nu)}, \tag{3.22}$$

where c is disk radius, d is disk thickness, ν is Poisson's ratio, and P is the hydraulic pressure.

Figure 3.14 compares stress profiles of the pressure-on-ring test and the ring-on-ring test. Disk surface displacement and comparison of experimental and calculated stresses are given by Salem et al.[15,16,17] The closer the support radius is to the disk radius, the more failure occurs at the support. In experiments with 6-mm-thick glass disks with a 25 mm diameter, the fraction of support failures decreased from 25% to 5% when the support diameter was reduced from 23 to 20 mm.

The deflection of the tensile face of the disk, as a function of radial distance r from the center, is[18]

$$\text{Deflection} = \frac{3Pb^4(1-\nu^2)}{16Ed^3}\left[\frac{2(1-\nu)b^2}{(1+\nu)c^2}\left(1-\frac{r^2}{b^2}\right) + 4\left(1-\frac{r^2}{b^2}\right) - \left(1-\frac{r^4}{b^4}\right)\right], \tag{3.23}$$

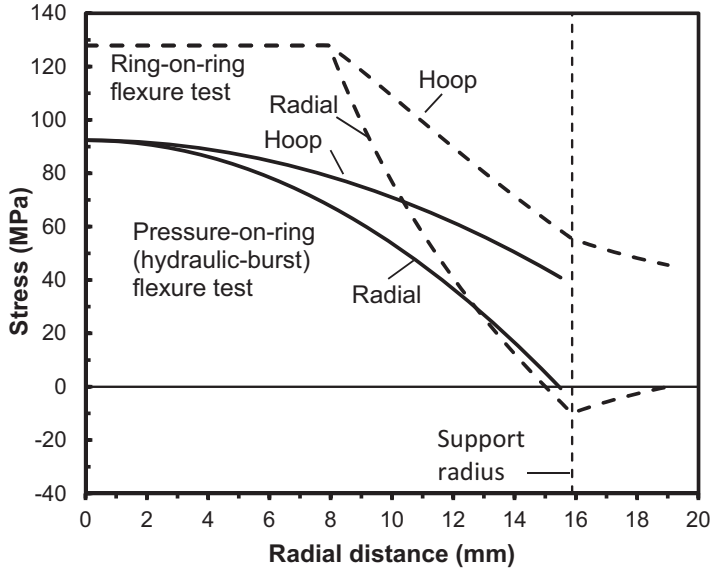

Figure 3.14 Radial and hoop stresses on lower surface of a disk in the pressure-on-ring test with $b = 15.875$ mm, $c = 19$ mm, $d = 2$ mm, $\nu = 0.27$, $P = 1.26$ MPa $= 12.6$ bar. Dashed lines are from Fig. 3.12 for the same size disk with a load of 1000 N applied to the load ring.

where E is Young's modulus. If hydraulic-burst pressure were raised to 1.748 MPa in Fig. 3.14, the stress at the center of the disk would be equal to the maximum stress in the ring-on-ring flexure test. Inserting $P = 1.748$ MPa and $E = 272$ GPa into Eq. (3.23) gives a maximum deflection of 34 μm at $r = 0$ with parameters in Fig. 3.14. For the same maximum stress, the deflection in the ring-on-ring test was 58 μm in the previous example. The ring-on-ring test produces greater deflection than the pressure-on-ring test at the same maximum stress.

In a study of the hydraulic-burst (pressure-on-ring) test in Fig. 3.13, 39 disks of high-purity, opaque, as-fired polycrystalline alumina were tested to failure.[19] "As-fired" means that the surfaces were not ground or polished. They were used as they came out of the sintering furnace. All disks had a nominal thickness of 0.635 mm.

One set of 39 disks had a diameter ($2c$ in Fig. 3.13) of 25 mm and another set had a diameter of 20 mm. In both cases, the support diameter $2b$ was 80% of the disk diameter; therefore, the support ring was located 2 mm from the edge of the 20 mm disks and 2.5 mm from the edge of the 25 mm disks. The support ring was covered by a 0.05-mm-thick copper washer whose ductility reduces flatness problems and contact stress.

In the case of the 20 mm disks, 4 of 39 specimens failed at the edge and 10 failed at the support radius. For the 25 mm disks, 1 of 39 disks failed at the edge and no disks failed at the support radius. The large number of edge and support ring failures when the support ring was just 2 mm from the edge should be a caution not to design pressure-on-ring windows with the support ring too close to the edge. It would have been good to test the reproducibility of these observations with two more sets of disks, but that was not possible.

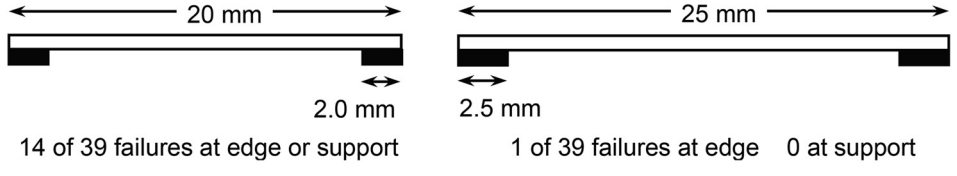

3.2.5 Stronger ceramics tend to break into more pieces

Figure 3.15 shows two ceramic disks that were broken in ring-on-ring flexure. The disk on the right broke at 1.4 times as much load as the disk on the left. It is typical that the stronger sample broke into more pieces because it stored 40% more elastic potential energy than the weaker sample prior to shattering. The dashed lines in Fig. 3.15 show the positions of the load and support rings. In the disk on the right, much damage is observed beneath

Example: Predicting flexure strength for components with different sizes

Zinc sulfide disks in Fig. 4.4 with an effective area of 2.65 cm^2 have an observed mean strength of $S_1 = 92.8$ MPa with a Weibull modulus of 4.67. Predict the mean strength of the same quality of material with an effective area of 100 cm^2 under tensile stress. We answer this question with Eq. (4.22):

$$\frac{S_2}{92.8\,\text{MPa}} = \left(\frac{2.65\,\text{cm}^2}{100\,\text{cm}^2}\right)^{1/4.67} \Rightarrow S_2 = 43\,\text{MPa}$$

We predict that the 100-cm^2 specimens will fail at a mean stress of 43 MPa, which is less than half the strength of the 2.65-cm^2 specimens. The greater the Weibull modulus, the less the mean strength depends on area. If $m = 10$, we would predict that the mean strength of the large specimens would be 65 MPa.

Figure 4.8 confirms the strength-scaling relation in Eq. (4.22). Taking the base 10 logarithm of both sides of the equation gives

$$\log S_2 = -\frac{1}{m}\log\left(\frac{A_2}{A_1}\right) + \log S_1. \tag{4.23}$$

We can measure the mean strengths S_2 of sets of samples with a different effective area A_2 for each set. Taking $A_1 = 1$ cm^2, Eq. (4.23) predicts that a graph of $\log S_2$ versus $\log(A_2/A_1)$ will be a straight line with a slope of $-1/m$ and a y-intercept of $\log S_1$ when $\log(A_2/A_1) = 0$ (that is, when $A_2 = 1$ cm^2). From the slope in Fig. 4.8, $m = -1/(-0.0640) = 15.6$. From the intercept in Fig. 4.8, the predicted strength for an area of 1 cm^2 is $10^{2.4809} = 303$ MPa.

4.7 Weibull Probability of Survival Without Slow Crack Growth

How can we use the Weibull equation to predict the probability of survival of a window made from a material whose strength we have measured with coupons? Consider the transparent polycrystalline alumina window in Fig. 4.9 held in a frame by a compliant gasket with a pressure difference $P = 0.5$ MPa (5 bar) across the window. The right side of the window becomes convex and is placed in tension.

You might recognize the window in Fig. 4.9 as an example of the pressure-on-ring burst test in Fig. 3.13. Tensile surface stresses shown in Fig. 4.9 are computed with Eqs. (3.21) and (3.22) from the parameters in the figure caption. The maximum stress at the center of the tensile surface of the window in Fig. 4.9 with a pressure difference of 0.5 MPa (5 bar, 5 atm) computed with

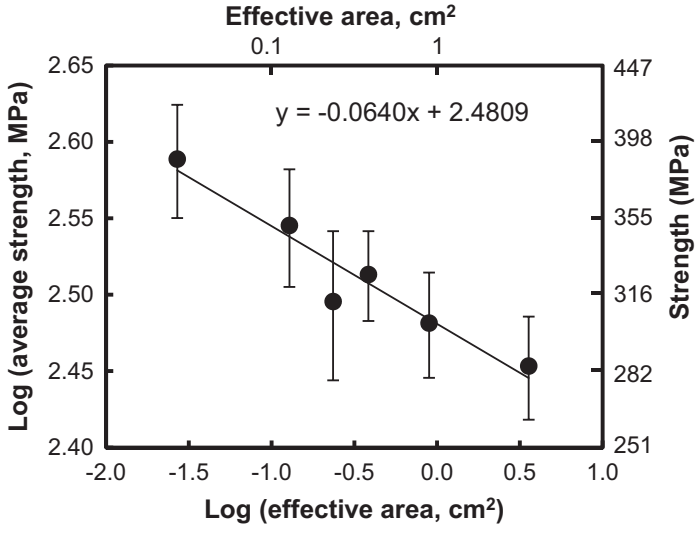

Test and sample type*	Number of specimens	Average strength (MPa)	Standard deviation (MPa)	Weibull modulus for set	Effective area (cm^2)
3-point size A	18	388	33	14.6	0.0269
4-point size A	17	313	35	9.4	0.235
3-point size B	18	351	31	12.2	0.128
4-point size B	48	303	24	14.3	0.894
3-point size C	18	326	22	16.4	0.384
4-point size C	18	284	22	14.5	3.57

*Specimen sizes A, B, and C are described in Table 3.1

Figure 4.8 Demonstration of Weibull area scaling for 3- and 4-point flexure bars made of sintered silicon carbide. (Data from C. A. Johnson and W. T. Tucker in ASTM C1683-10.)

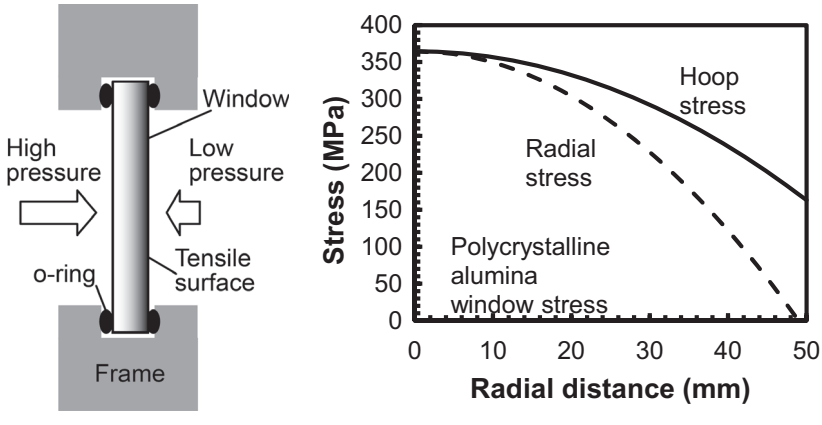

Figure 4.9 Window in a frame with pressure difference $P = 0.5$ MPa across the window. Window radius $c = 55$ mm, support radius (o-ring radius) $b = 50$ mm, window thickness $d = 2$ mm, Poisson's ratio $\nu = 0.24$, and Young's modulus $E = 403$ GPa. Radial and hoop surface stresses are computed with Eqs. (3.21) and (3.22).

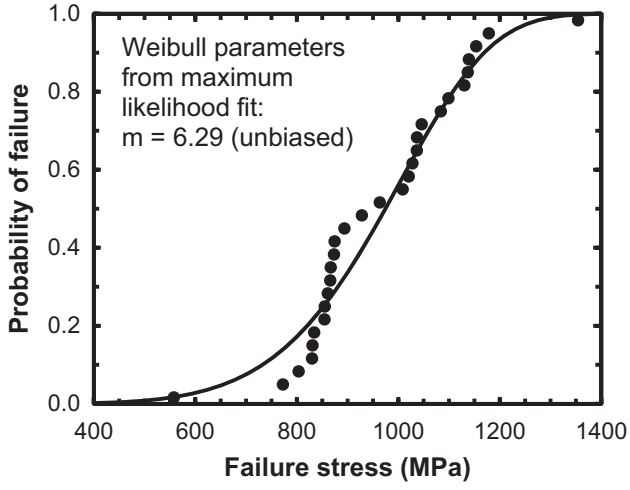

Figure 4.10 Weibull plot of strengths of 30 transparent polycrystalline alumina disks with radius 19.0 mm and thickness 2.00 mm using a ring-on-ring test fixture with load radius 7.94 mm and support radius 15.88 mm tested in air at ~45% relative humidity at ~24°C with crosshead speed 0.508 mm/min. Smooth curve is fit to Weibull Eq. (4.1). (Data from CeraNova Corp.)

Eq. (3.21) at $r = 0$ is 365 MPa. Poisson's ratio and Young's modulus given in the caption of Fig. 4.9 apply to a fine-grain polycrystalline alumina (grain size 0.3–0.4 μm) that is transparent in the midwave infrared region and visibly translucent because of optical scatter.[7,8,9,10,11,12]

Figure 4.10 shows the strengths of 30 coupons of polycrystalline alumina tested in ambient atmosphere in ring-on-ring flexure. Other experiments that are not shown suggest that slow crack growth in polycrystalline alumina at ambient humidity near room temperature is negligible. The pattern of points in the Weibull plot suggests that there are at least two different populations of flaws giving rise to mean strengths near 850 MPa and 1100 MPa. Exhaustive fractography was not performed, so there is not enough information to categorize the flaws. We choose to describe the entire data set with a single Weibull modulus m and characteristic strength σ_θ. Two of the 30 specimens failed in the outer gage section (between the load and support rings) at stresses of 803 and 1153 MPa. These are the third-lowest and third-highest points in Fig. 3.33, and there is no reason to discard these points from the Weibull analysis. It is a good reminder that the failure stress in Weibull analysis is the maximum stress inside the load ring.

Weibull analysis by the maximum-likelihood method in Section 4.4 gives an unbiased Weibull modulus of $m = 6.29$ with a 90% confidence range of 4.72 to 7.69. The characteristic strength is $\sigma_\theta = 1030$ MPa. With $m = 6.29$, we compute the test coupon effective area $A_e = 5.54$ cm^2 with

a 2–3 mm dome thickness. In lower-speed launches, the temperature gradient is smaller. It is common for the temperature at maximum stress to lie between 25° and 500°C. The thermal shock figure of merit near 300 K in Table 5.2 roughly provides an appropriate qualitative comparison of materials.

The thermal shock figure of merit is only a semi-quantitative indicator that is helpful in material selection. *To assess the probability of survival of a dome or window for a particular application, there is no substitute for a careful finite element aerothermal stress analysis using the best available temperature-dependent data for the material to be employed.* Such an analysis should include the attachment of the dome to the airframe because high stress can occur at the attachment. Weibull analysis, described in Section 4.8, can be used to predict the probability of survival of the dome or window once the stress distribution is calculated. Weibull parameters might need to be measured for the material of interest at the temperature of interest. It is rare that a high degree of confidence can be attached to the results of thermal stress analysis coupled with Weibull probability of survival because of uncertainty in every part of the analysis.

The wind tunnel in Fig. 5.16 allows the performance of a missile dome to be measured in a flight-like environment.[60] Hot air is created by burning hydrogen in a high-speed stream of air. Temperature and air pressure at the surface of the dome are independent variables. After establishing the desired flow, a mounted dome can be rapidly inserted into the flow. Alternatively, a covered dome can be in the flow the whole time and the cover quickly removed when required flow conditions are attained. The inside surface of a dome can be instrumented to measure strain and temperature as the dome is heated.

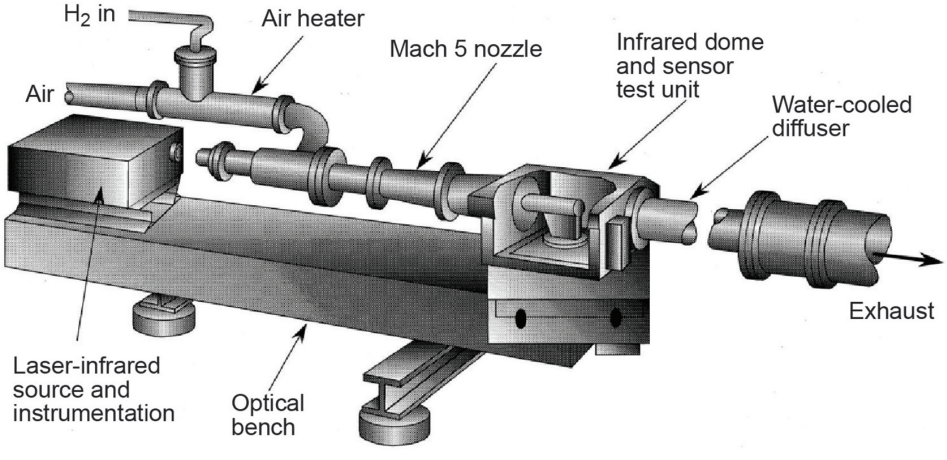

Figure 5.16 Aerothermal/Infrared Test Facility formerly at the Johns Hopkins University Applied Physics Laboratory, Laurel, Maryland. (Reprinted from Lin and Weckesser,[60] © 1992 The Johns Hopkins University Applied Physics Laboratory LLC. All Rights Reserved.)

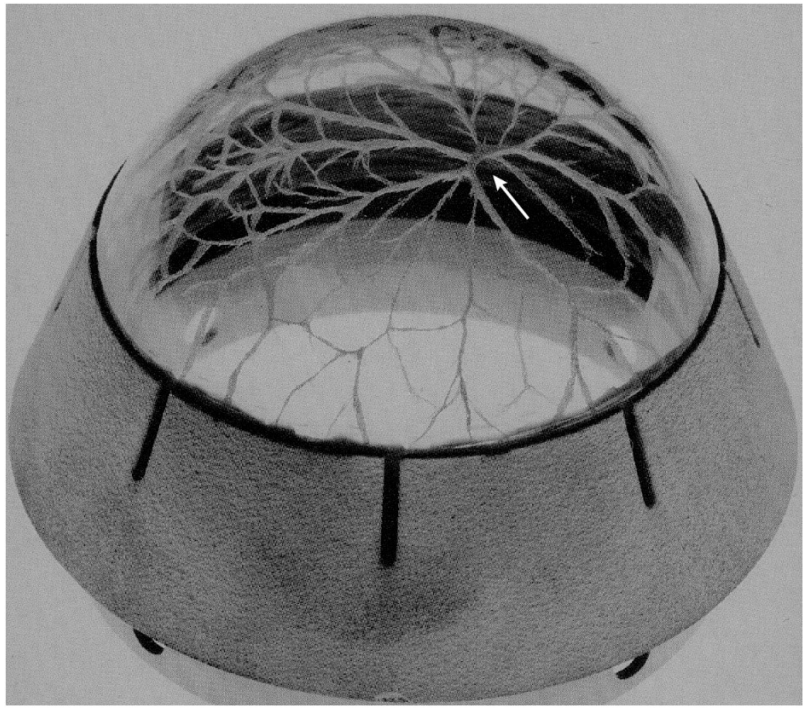

Figure 5.17 Fracture pattern in spinel dome after exposure to a Mach 4.6 airstream with a total pressure of 6.2 MPa and a total temperature of 1390 K. (Reprinted from Lin and Weckesser,[60])

Figure 5.17 shows the fracture pattern in a spinel dome shattered from thermal shock in the wind tunnel. The arrow points to the likely location of the fracture origin. Compare the dome fracture pattern with representative disk fracture patterns in Fig. 3.18 and see if you agree with where I drew the arrow. Would you say that this dome is of low, moderate, or high strength for a spinel dome? (I say high.)

The wind tunnel created a Mach 4.6 airstream with a total pressure of 6.2 MPa and a total temperature of 1390 K. Total temperature T_{stag} at the stagnation point on the nose of the dome is the sum of the free-stream temperature of air T_∞ plus the dynamic temperature when air comes to rest at the nose of the dome. The relation of T_{stag} to T_∞ is given by Eq. (5.23). Total pressure P_{stag} at the stagnation point is the sum of the free-stream pressure P_∞ plus the dynamic pressure when air comes to rest at the nose of the dome, as given by Eq. (4.35).

Figure 5.18 compares the observed and predicted stress in a dome during a wind tunnel test. The stress in a lanthana-doped yttria dome was measured by strain gauges and calculated by finite element methods. The dome shattered

5.6 Aerodynamic Domes

The ability of a rocket engine to fly fast readily exceeds the ability of most infrared windows to survive thermal shock. Diamond is an exception that can probably withstand the thermal stress of any tactical missile flight because the high thermal conductivity of diamond does not permit much temperature difference to occur. Several approaches can be taken to promote window survival. The window could be actively cooled by blowing cold gas over the exposed surface. However, mixing of cold gas with hot air creates fluctuations in density and refractive index that might blur the scene being viewed. This effect is called *aero-optic distortion*. Another idea is to pass coolant through channels in the window, as in Fig. 2.39. Disadvantages of this scheme include blockage of the scene by the channels, wavefront distortion by temperature gradients in the window, reflections and diffraction from the channel walls, and emittance from the coolant. Active cooling adds weight, volume, and complexity to the system.

We saw in Fig. 5.15 that the temperature on a dome falls rapidly as we move off the nose (if the flow remains laminar). One way to take advantage of this effect is to mount a flat infrared window on the rear portion of a structural dome, as in Fig. 5.20(a). Such a window does not get very hot, but the field of view is limited compared to that of a nose-mounted hemispheric dome. An additional advantage of the slanted window is that its angle of attack is always far from perpendicular to the airstream, so it can survive impacts with raindrops and solid particles.

The faceted dome in Fig. 5.20(b) is an 8-sided pyramid with spinel panes and a heat-resistant metal nose tip.[61] The French Mistral missile has a similar dome with magnesium fluoride panes. The faces of the pyramid remain much cooler than the nose of a hemisphere. The aerodynamic design reduces drag and thereby increases range, speed, or payload. The biggest disadvantage of the design is the multiple internal reflections of sunlight that lead to glint whenever the sun is in the forward hemisphere of view. Joining of the panes and overall cost are also significant considerations in this design.

A next step after a pyramid in aerodynamic dome design is the tangent ogive (pronounce ō-jive) dome in Fig. 5.21, whose low drag enables some combination of increased range, speed, or payload for a missile.[62,63] Like the pyramidal dome, the ogive requires a heat-resistant nose tip. The ogive shape distorts the image of the outside world and requires some form of optical correction, such as the notional arch corrector in Fig. 5.21.[64] The ogive dome in Fig. 5.21 is made from polycrystalline alumina, which has the same chemical composition as sapphire (Al_2O_3) with similar physical properties and durability and high thermal shock resistance. Polycrystalline alumina has good midwave infrared transmittance (Fig. 1.26) but is translucent at visible wavelengths (Fig. 1.24) because of optical scatter from its birefringent grains.

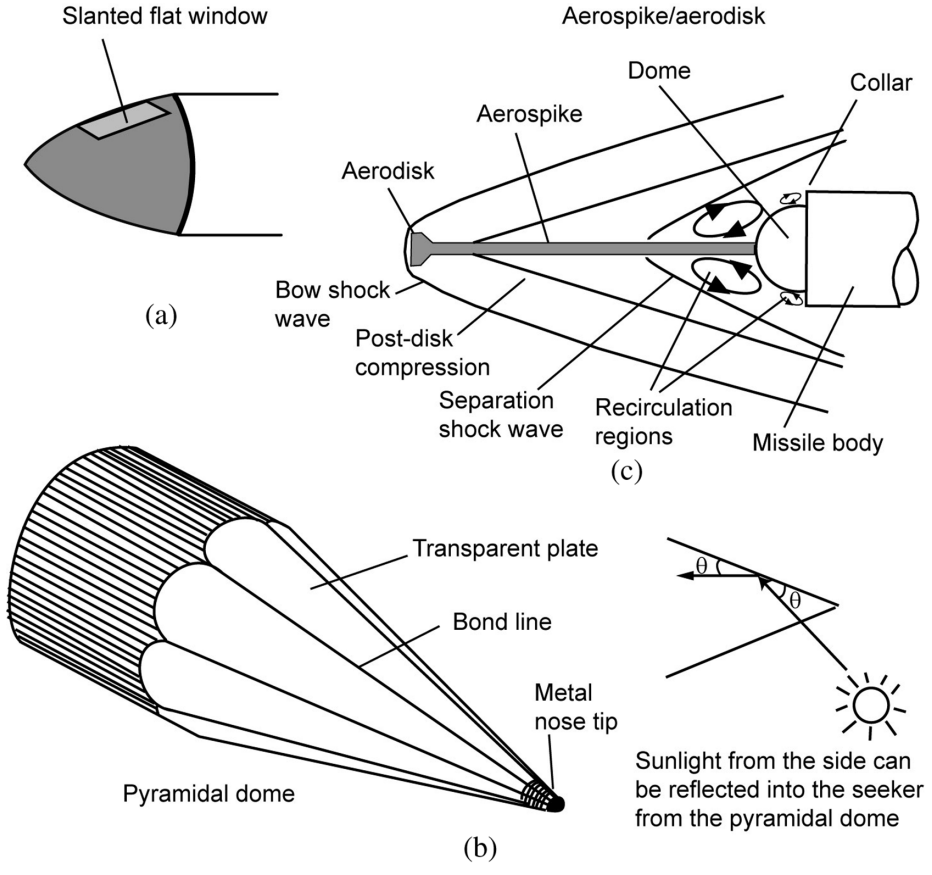

Figure 5.20 Aerodynamic domes.

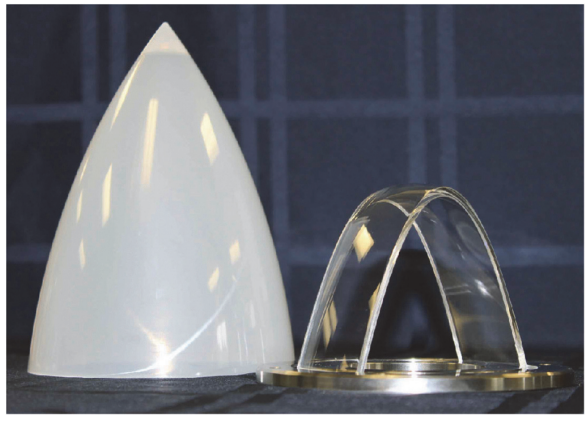

Figure 5.21 Polycrystalline alumina aerodynamic dome with notional arch corrective optic. The alumina dome blank was fabricated by CeraNova Corp. (Marlborough, Massachusetts) and ground and polished by OptiPro Systems (Ontario, New York). (Photograph credit: OptiPro.)

The aerospike/aerodisk in Fig. 5.20(c) reduces drag and deflects the bow shock from the hemispheric dome.[65] The collar created by the missile body that is wider than the dome prevents reattachment of the shock wave onto the dome at low angles of attack. Wind tunnel tests of the aerospike/aerodisk in Fig. 5.22 show that the shock wave reattaches to the dome at angles of attack greater than 5 deg. Reattachment generates higher temperature and pressure on the side of the dome than would be found at the nose of the dome in the absence of a spike.

Figure 5.23 shows a 2.5-mm-thick flat window mounted at an angle of 6 deg from horizontal on the structural dome of a high-speed missile operating at sea level.[66,67,68] The low angle of incidence with the airstream reduces aerodynamic heating. The missile is fast enough that the recovery temperature at the window 0.7 s after launch is 1400°C and the peak cold wall heat flux is 310 W/cm^2. (Recovery temperature is the temperature in the boundary layer of air adjacent to the surface of the window.) The window transmits at 1.09 μm for laser guidance. Analysis of sapphire and fused silica (results are in Table 5.6) showed that fused silica was the material that could survive the mission, despite having a 700 K temperature difference between the outside and inside surfaces and despite having only one-sixth of the strength of sapphire. Fused silica has a large temperature difference because it has low thermal conductivity. However, the stress in fused silica is only 2% as great as the stress in sapphire because fused silica has low thermal expansion and low Young's modulus. Low expansion creates little strain and low Young's modulus gives little stress from the little strain.

Windows on some high-speed missiles are protected by a durable shroud that must be jettisoned after the stressing part of a flight. The process of removing the shroud must not allow the shroud to impact the missile aft of the window. Some windows on low-speed missiles have been protected by a frangible dome cover, which is a pre-stressed glass material that shatters into fine particles when it is sharply impacted to remove the cover.

5.7 Thermal Stability of Window Materials

Even if a window or dome is heated gradually so that thermal shock is not a concern, every material has an upper operating temperature above which it cannot be used. The temperature might be dictated by loss of strength or loss of optical transmission (giving increased emission) resulting from reversible physical changes (such as free-carrier absorption in Section 1.12) or irreversible chemical changes. A material might be usable at a particular temperature for the short duration of a missile flight, but not usable for a longer period at the same temperature. Few data exist in the literature to establish upper operating temperatures for short-duration exposure.

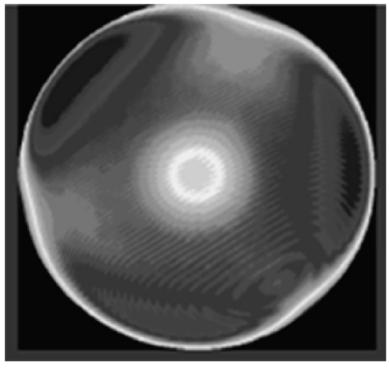

Figure 7.14 Convex surface map of a dome constructed by stitching together overlapping circular regions. For the entire surface, peak-to-valley figure error is 1.05 μm (1.65 λ) with root-mean-square error 0.118 μm (0.187 λ). Total measurement time was 12 min. (Figure courtesy of QED Technologies, Rochester, New York.)

7.4.2 UltraSurf optical coordinate measuring machine

UltraSurf from OptiPro Systems (Ontario, New York) is a noncontact coordinate measuring machine that uses light instead of mechanical contact to locate points on the surface of optics of a wide variety of shapes.[25,26,27,28,29,30] Figure 7.15 shows UltraSurf measuring the inside and outside of an ogive

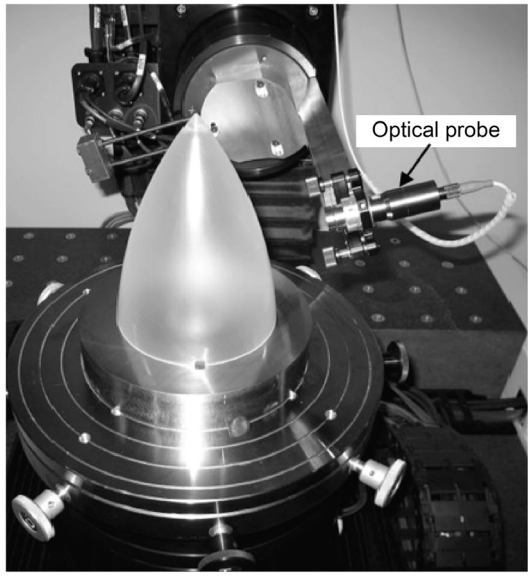

Figure 7.15 UltraSurf metrology instrument measures outer surface of a fine-ground ogive dome with a white light chromatic confocal optical probe, keeping the probe perpendicular to the surface at each point. A low-coherence interferometry probe operating at 1.31 μm can find the distance from the probe to the outer and inner surfaces to map both surfaces and thickness in one measurement. The instrument has five mechanical degrees of freedom to move the workpiece and the probe. (Photograph courtesy of OptiPro Systems, Ontario, New York.)

dome to map both surfaces and the thickness prior to final figure correction and optical polishing. An example of a finished dome was shown in Fig. 5.21. Some models of UltraSurf can measure optics with diameters up to ~300 mm and height up to ~500 mm.

An ogive has rotational symmetry, but grinding and polishing leave some irregularities that are not rotationally symmetric. To make optical figure corrections, it is necessary to remove material from local regions. In one example of finishing an ogive, rotationally symmetric finishing reduced the peak-to-valley (p-v) figure error from 8.4 to 6.6 μm and the rms error from 1.89 to 1.02 μm. In the next polishing step, local, non-rotationally symmetric corrections reduced the p-v figure error to 4.15 μm and the rms error to 0.53 μm. Metrology identified high regions and then polishing improved those specific regions.

Multiple probes can be used on UltraSurf, but two are most common. Figure 7.16 is a schematic view of a Marposs STIL white light chromatic confocal optical probe,[31] which is used for accurate measurement of the outer surface of an optic.[26] The probe can measure ground surfaces with high optical scatter and it can measure polished surfaces with low scatter. The probe's 25 deg tolerance for off-normal reflected light is especially helpful for measuring a rough surface.

White light enters the probe in Fig. 7.16 through a fiber optic cable. Optics inside the probe separate the light into its component wavelengths in the form of a conical beam emerging from the exit of the probe. At the centerline of the

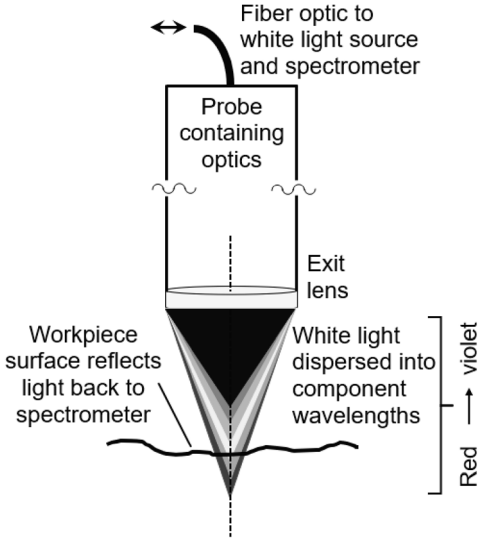

Figure 7.16 Schematic diagram showing operation of a Marposs STIL white light chromatic optical probe used on UltraSurf for accurate measurement of coordinates on the outer surface of a workpiece.

Chapter 9
Erosion and Impact Protection

One of the greatest challenges in the use of infrared windows and domes is to protect them from damage by particle impact. Collisions with raindrops are a problem at the velocities of airplanes and missiles. Figure 9.1 shows the damage to a missile dome after traversing a rainfield on the rocket sled shown in Fig. 9.2.[1,2] Bug impacts at high speed can also damage infrared windows (Fig. 9.3) Blowing sand is harmful in high- or low-speed collisions. This chapter describes the effects of rain and sand impact, discusses laboratory

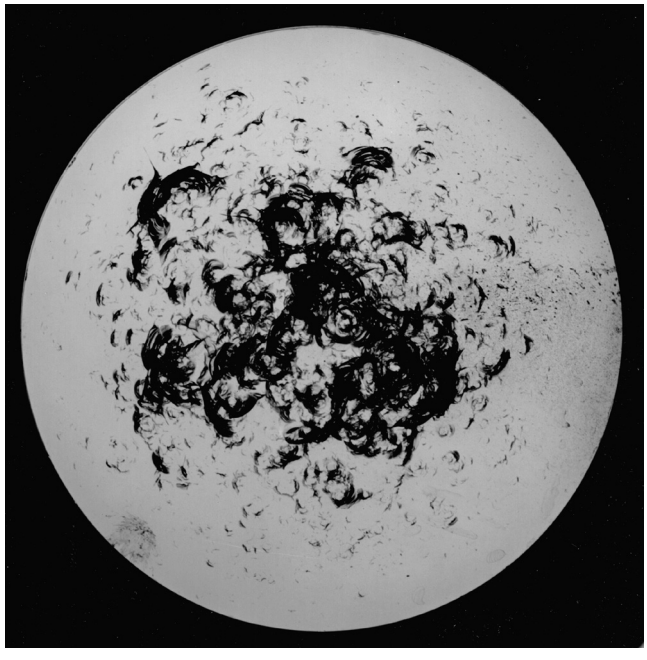

Figure 9.1 Waterdrop impact damage on a Corning 0160 glass missile dome that traversed a 760-m-long artificial rainfield (4.6 cm/h rainfall rate, average drop diameter $<$0.5 mm) at Mach 1.4 on the rocket sled in Fig. 9.2.[1] Notice that damage is concentrated at the center where the impact angle is near normal. (Photograph courtesy of Naval Air Warfare Center, China Lake.)

Figure 9.2 *Upper:* Dome mounted on a rocket sled at the Supersonic Naval Ordnance Research Track (SNORT) at the Naval Air Warfare Center at China Lake.[1] *Lower:* Spray heads used to create an artificial rainfield. (Photographs courtesy of Naval Air Warfare Center, China Lake.)

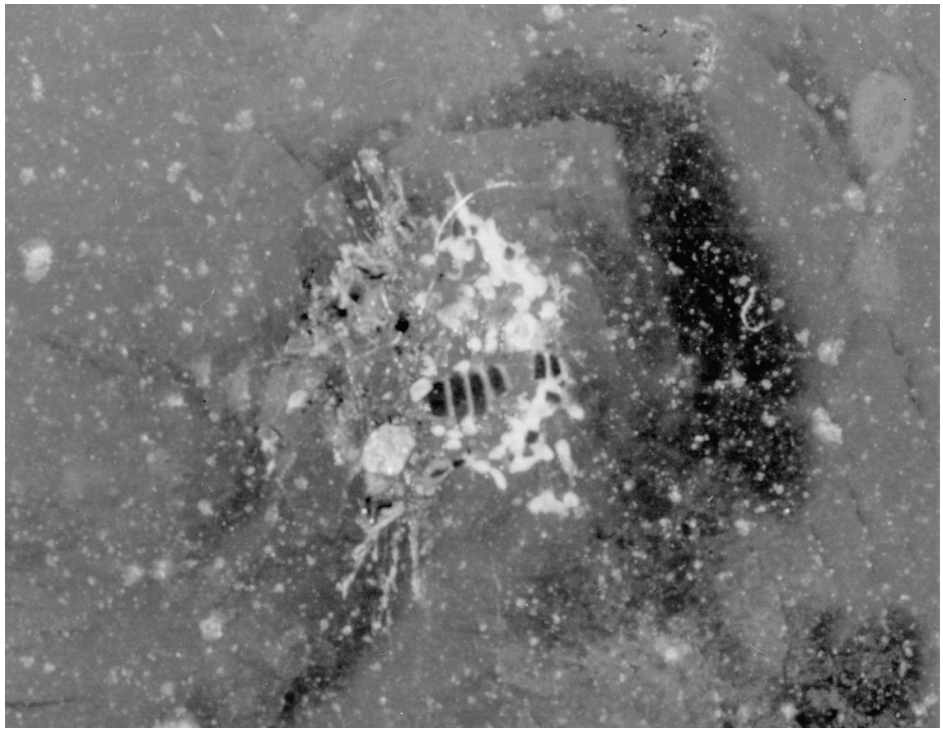

Figure 9.3 Insect impact damage in a composite ZnS|ZnSe LANTIRN window. (Photograph courtesy of Nora Osborne, University of Dayton Research Institute.[3])

impact tests, and reviews work on coatings used to improve window durability.

A report on failure mechanisms in LANTIRN sensor windows is instructive.[3] LANTIRN was the *L*ow-*A*ltitude *N*avigation *T*argeting *I*nfra-*R*ed *N*ight pod system carried by aircraft. The pod has a trapezoidal Tuftran® window (Fig. 6.27) with approximate dimensions of 119×150 mm consisting of 6.6 mm of ZnSe overgrown with 1.0 mm of ZnS deposited by chemical vapor deposition. There are antireflection coatings on both sides of the window. A 1992 report stated that of 1100 windows delivered to the U.S. Air Force, $\sim$200 had been condemned and removed from service. Of the condemned windows, two-thirds had experienced catastrophic failure, often with multiple types of damage evident. Twenty-eight percent of the windows had moderate to severe sand erosion, 14% had moderate to severe rain erosion, 29% had obvious insect strikes, and 13% of all failures were directly attributed to insect strikes. Forty-two percent of the windows had surface discoloration or etching attributed to chemicals in the atmosphere.

The LANTIRN window has some residual tensile stress ($<$10 MPa) due to thermal expansion mismatch between ZnSe and ZnS (Figs 8.21 and 8.23).

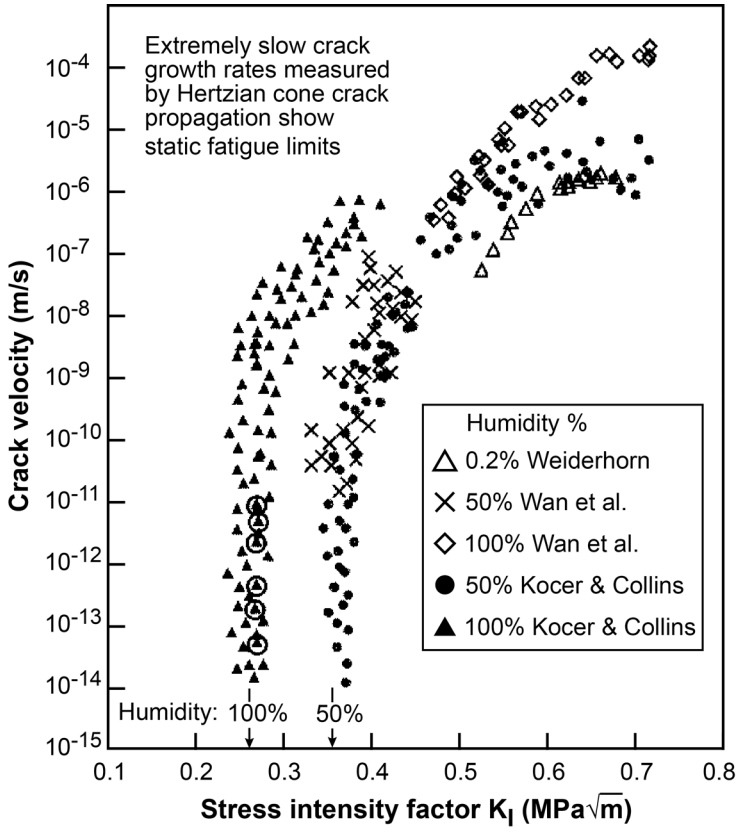

Figure 10.6 Fatigue limits for soda-lime silicate glass in 100% and 50% humidity. Kocer and Collin room temperature slow crack growth rate in soda-lime silicate glass measured by stable growth of Hertzian cone cracks induced by indentation with a blunt, hardened steel cylindrical punch with a diameter of ~0.6 mm. Multiple crack velocities are measured from a single coupon. Six circled triangles at the lower left demonstrate reproducibility from a single coupon. There is more scatter between different coupons. The graph shows previous measurements at higher crack velocities made by Wan et al.[23] and by Wiederhorn.[3] The blunt indentation method for measuring slow crack growth rate was introduced by Swain and Lawn in 1973.[24] (Adapted from Kocer and Collins[22] with permission of Wiley.)

interpretation that I would not rely on. Even if there is a "threshold" strength, it might not necessarily apply to other BK7 material that is not ground and polished identically to the coupons in Fig. 4.31.

10.1.3 Effect of humidity and temperature on slow crack growth[25]

The classic study of crack propagation in glass by Sheldon Wiederhorn[26] at the U.S. National Bureau of Standards is summarized in Fig. 10.7.[2,3] The observed crack velocity is plotted as a function of K_I calculated with Eq. (10.2). The crack velocity curves can be divided into three general regions:

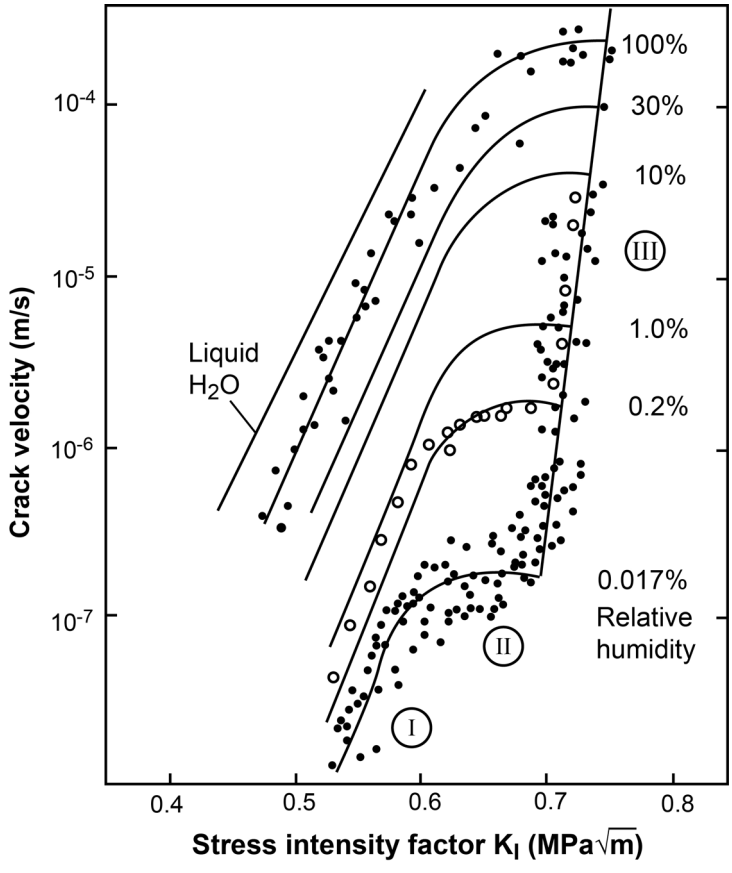

Figure 10.7 Wiederhorn's classic diagram[2] showing crack velocity in soda-lime silicate glass in humid N_2 and in liquid water. Crack growth regions I, II, and III are highlighted in circles. Humidity ranges from 0.017% to 100%. Some points are shown to indicate the spread of the data. The full graph was derived from ~1000 points.

1. In region I of Fig. 10.7 (the linear lower left portion of each curve), crack velocity is exponentially dependent on the stress intensity factor and increases as humidity in the test atmosphere increases. Crack velocity is greatest when the specimen is immersed in liquid water (upper left curve). The rate of crack growth in region I is governed by the rate of the stress-enhanced chemical reaction of water with glass at the crack tip.[2,3]
2. In region II, crack velocity is independent of the stress intensity factor but is strongly dependent on humidity. Crack velocity in region II is governed by the rate at which water diffuses to the crack tip to react with the glass.[2,3]

3. In region III, crack velocity is again exponentially dependent on the stress intensity factor but is independent of the concentration of water in the environment. The rate of crack growth is controlled by the chemical composition and structure of the glass. Crack velocity may be so rapid in region III that fracture is essentially instantaneous.[2,3]

The ability of water to enhance crack propagation under applied stress is called *stress corrosion*. A possible mechanism by which water reacts with glass at the tip of the growing crack is shown in Fig. 10.8.[27,28] In region I of Fig. 10.7, crack velocity increases with increasing temperature and with increasing pH (increasing OH^- concentration) if the glass is immersed in aqueous solution.

Increasing temperature increases the rate of slow crack growth in nearly all brittle materials. The effect of temperature on crack growth rate in soda-lime silicate glass in water is shown in Fig. 10.9.[10] The linear portion of the curve for region I crack growth is fit by an empirical equation of the form[29]

Effect of temperature on crack velocity

$$v = v_0 \cdot e^{(-E^* + bK_I)/RT}, \tag{10.5}$$

where E^* is interpreted as the *activation energy* (J/mol) that must be supplied for chemical bond breaking. K_I is the stress intensity factor with units $Pa\sqrt{m}$ (not $MPa\sqrt{m}$), R is the gas constant [8.31446 J/(mol · K)], and T is temperature (K). Units of v_0 are m/s. Units of b are $(m^{5/2}/mol)$ required to make $(bK_I)/(RT)$ dimensionless. Parameters E^*, v_0, and b are derived from fitting measured data.

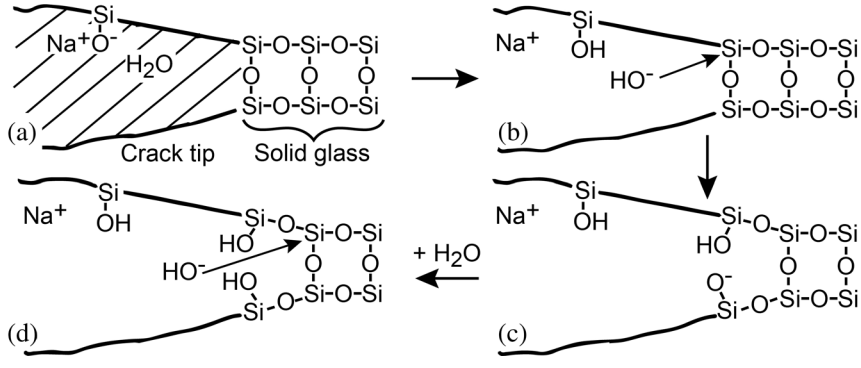

Figure 10.8 Proposed mechanism[27,28] for stress corrosion in glass. In going from step (a) to step (b), H_2O reacts with $–SiO^-Na^+$ on the glass surface to produce –SiOH and Na^+OH^-. In step (c), OH^- breaks a –Si–O–Si– bond at the crack tip. In step (d), another H_2O reacts with $–SiO^-$ generated in step (c) to create another OH^- that can attack another –Si–O–Si– bond at the crack tip.